Effect of microporous layer structural parameters on heat and mass transfer in proton exchange membrane fuel cells

Zhang, Zhenya; Mao, Jia; Wei, Houyu; Cheng, Chuanxiao; Liu, Zhengxuan

DOI
10.1016/j.applthermaleng.2023.122083

Publication date
2024

Document Version
Final published version

Published in
Applied Thermal Engineering

Applied Thermal Engineering 239 (2024) 122083

Contents lists available at ScienceDirect

Applied Thermal Engineering

journal homepage: www.elsevier.com/locate/apthermeng

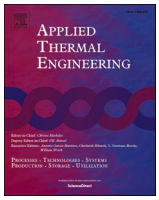

Research Paper

Effect of microporous layer structural parameters on heat and mass transfer in proton exchange membrane fuel cells

Zhenya Zhang [a], Jia Mao [a], Houyu Wei [a], Chuanxiao Cheng [a], Zhengxuan Liu [b,*]

[a] School of Energy and Power Engineering, Zhengzhou University of Light Industry, Zhengzhou, 450001, China
[b] Faculty of Architecture and the Built Environment, Delft University of Technology, Julianalaan 134, 2628 BL, Delft, Netherlands

ARTICLE INFO

Keywords:
Proton exchange membrane fuel cells
Microporous layer
Heat and mass transfer
Performance optimization
Fuel cell efficiency

ABSTRACT

Proton exchange membrane fuel cells offer promising clean energy solutions for various applications. However, their performance relies heavily on the properties of the microporous layer, which plays a crucial role in transporting and distributing the components in the fuel cell. To date, the potential for optimising the microporous layer material structural parameters to enhance the fuel cell performance remains largely unexplored. This study aims to fill this research gap by conducting a comprehensive investigation of the effects of different microporous layer material structural parameters on the heat and mass transfer in the membrane electrode assembly. MATLAB was used for optimising the performance of the fuel cell components. The results show that increasing the microporous layer thickness from 5 to 50 μm significantly affects the species transport, leading to a substantial reduction in the molar fraction of H_2 and O_2 at the electrochemical reaction sites. Furthermore, the distribution of the liquid water saturation inside the fuel cell is influenced by the porosity and permeability of the microporous layer. By increasing the porosity from 0.3 to 0.6, the liquid water saturation at the interface of the catalyst layer and microporous layer decreases by 0.52 % and 1.12 % at output voltages of 0.5 V and 0.7 V, respectively. This reduction enhances the efficiency of internal water transport. Moreover, reducing the permeability of the microporous layer from 2×10^{-12} to 1×10^{-13} at 0.5 V and 0.7 V leads to an increase in liquid water saturation at the interface of the proton exchange membrane and the catalyst layer by 1.49 % and 0.74 %, respectively, causing hindrance to the transport of internal liquid water. This study provides valuable insights into the interplay between the properties of the microporous layer material properties and heat and mass transfer characteristics in proton exchange membrane fuel cell.

1. Introduction

With the dynamic and fast-paced advancements in the energy industry, hydrogen energy has garnered considerable attention as a highly promising solution in the global energy landscape, and it is a key contender for the development of future energy carriers [1,2]. Proton exchange membrane fuel cells (PEMFCs) have emerged as an established technology for efficient energy conversion in hydrogen-based applications, offering distinct advantages such as exceptional power density, environmentally benign byproducts, and rapid start-up capabilities [3,4]. By operating through electrochemical reactions, PEMFCs facilitate the consumption of hydrogen at the anode and oxygen at the cathode, thereby converting chemical energy into electrical power. Consequently, their applicability spans across diverse domains, including new energy vehicles, stationary power plants, and portable electronic devices [5,6]. In recent years, PEMFCs have witnessed significant advancements and widespread implementation, driven by a persistent commitment to technological innovation.

Notably, improvements in the component materials, particularly the membrane electrode assembly (MEA), have enhanced the overall efficiency and reliability of PEMFCs [7]. The MEA, consisting of gas diffusion layers (GDLs), catalyst layers (CLs), and electrolyte membrane, plays a vital role in fuel cell performance [8,9]. Based on the five-layer MEA structure, researchers have investigated the effect of a microporous layer (MPL) inserted between the CL and GDL on the heat and mass transfer processes in the MEA. Compared with the porous-medium GDL, the MPL has smaller pores and has been proved to remarkably enhance the water removal performance of PEMFCs [10,11]. However, Karan et al. [12] and Atiyeh et al. [13] studied the water transport characteristics by adding MPL to the cathode. The results showed that the MPL did not increase back diffusion or improve the cathode water removal

* Corresponding author.
E-mail address: Z.liu-12@tudelft.nl (Z. Liu).

https://doi.org/10.1016/j.applthermaleng.2023.122083
Received 7 August 2023; Received in revised form 27 October 2023; Accepted 21 November 2023
Available online 24 November 2023

Nomenclature

Symbols

a	Active surface area density, m^{-1}
c	Gas concentration, $mol \cdot m^{-3}$
C	Specific heat, $J \cdot kg^{-1} \cdot K^{-1}$
D	Diffusion coefficient, $m^2 \cdot s^{-1}$
EW	Equivalent weight, $g \cdot mol^{-1}$
ΔG	Gibbs free energy difference, $J \cdot mol^{-1}$
h	Enthalpy, $J \cdot mol^{-1}$
i	Exchange current density, $A \cdot cm^{-2}$
I	Output current density, $A \cdot cm^{-2}$
j	Flux, $A \cdot m^{-2}$, $mol \cdot m^{-2} \cdot s^{-1}$, $W \cdot m^{-2}$
k	Thermal conductivity, $W \cdot K^{-1}$
K	Mass transport coefficients, $m \cdot s^{-1}$
L	Thickness, μm
M	Molar mass, $g \cdot mol^{-1}$
p	Pressure, Pa
R	Gas constant
RH	Relative humidity
s	Liquid water saturation
S	Source term
ΔS	Entropy change, $J \cdot mol^{-1} \cdot K^{-1}$
T	Temperature, K
u	Velocity
V	Molar volume, $m^3 \cdot mol^{-1}$

Greeks

α	Molar fraction of in dry gas
β	Half-fraction symmetry factor
γ	Phase change rate, s^{-1}
δ	Thickness, m
ε	Porosity
η	Overpotential, V
θ	Contact angle, °
κ	Permeability, m^2
λ	Ionomer water content
μ	Liquid water viscosity, Pa·s
ξ	Electro-osmotic drag coefficient
σ	Electron/protonic conductivity
τ	Pore tortuosity
ϕ	Potential, V
χ	Molar fraction of gas
ω	Mass Transfer Coefficient

Subscripts

abs	Absorption
ρ	Density, $g \cdot m^{-3}$
ad	Absorption/ Desorption
an	Anode
ca	Cathode
con	Condensation
des	Desorption
ec	Evaporation/ Condensation
eff	Effective
eq	Equilibrium
eva	Evaporation
env	Environment
H_2O	Water vapor
im	Immobile liquid water saturation
l	Liquid water
nor	Normal
red	Reduced
ref	Reference values
sat	Saturation
sim	Simulation

Abbreviations

CL	Catalyst layer
GC	Gas channel
GDL	Gaseous diffusion layer
H_2	Hydrogen
MEA	Membrane electrode assembly
MPL	Microporous layer
O_2	Oxygen
PEMFC	Proton exchange membrane fuel cell
RSME	Root mean square error

capability.

The ability of the MPL to substantially enhance the water removal performance has been recognised; however, there is a need to systematically investigate its influence on the overall fuel cell operation and efficiency. Some researchers have found that aside from enhancing the water transport performance, incorporating an MPL also plays a beneficial role in improving the electrical contact characteristics of the GDL and CL [14,15]. Li et al. [16] analysed a seven-layer MEA fuel cell under low relative humidity conditions and compared the effects of the stoichiometric ratio, operating pressure, and relative humidity on the I-V curve. The results demonstrated that membrane hydration can still be achieved when operating at high current densities under low relative humidity conditions. Zuo et al. [17] investigated the impact of the MPL on the operational degradation of PEMFCs. Through electrochemical impedance analysis, they discovered that at a low current (150 mA cm^{-2}), MPL exhibited a minor increase in the charge transfer resistance during the ageing process, indicating that the MPL can alleviate kinetic degradation. Additionally, an MPL with a smaller thickness and higher porosity were found to be more favorable for improving the fuel cell performance. Decreasing the MEA thickness is an inevitable trend, and optimising its thickness is one strategy for enhancing its overall performance. Zhou et al. [18] found that there is an optimal MPL thickness and thermal conductivity for improving the water management performance of the MEA.

Despite numerous studies on fuel cell performance, a comprehensive investigation of the influence of the MPL structural parameters on species transport kinetics is essential. The structural parameters of the MPL have a multifaceted impact on species transport. First, a thinner MPL is necessary to enhance the gas diffusion and water removal. Second, the MPL porosity and permeability positively affect gas transport. However, to maintain proton-exchange membrane wettability, increasing the thickness and reducing the porosity and permeability are required to boost the internal water content at low current densities or insufficient humidification. Therefore, there is significant interplay between the MPL structural parameters and MEA performance.

This study examines the impact of modifying the MPL structural parameters on heat and mass transfer from a single-factor perspective. In Section 3.2, the results of the numerical simulations that the effects of various MPL thicknesses on the distributions of H_2 at the anode side, O_2 at the cathode side, liquid water, water vapour, and temperature are discussed. Section 3.3 presents our findings on the influence of porosity and permeability on H_2, O_2, liquid water, and water vapour from a microscopic perspective. The primary objective of this study is to enhance the design of fuel cell assemblies by leveraging numerical simulation methods and conducting a comprehensive analysis of the fundamental theoretical principles. These insights are expected to play a

pivotal role in improving the thermal management performance of fuel cells and facilitate the development and application of efficient fuel cell systems.

2. Numerical model

This study applied a one-dimensional, steady-state, two-phase, non-isothermal numerical model developed and validated by Vetter and Schumacher [19] was referenced. Based on this foundational model, new boundary conditions were set using MATLAB to explore the impact of the MPL structural parameters on the heat and mass transfer processes in the MEA. The primary research objective of this study was to identify the key factors influencing these heat and mass transfer processes, providing insights into the improvement of fuel cell performance and its broader applications. A schematic of the MEA structure is depicted in Fig. 1.

2.1. Model assumptions

To simulate the transport phenomena inside the PEMFC, the MPL was treated as a separate computational domain, and all conservation equations were solved. Throughout the research process, several assumptions and model simplifications were applied to ensure computational feasibility and facilitate analysis. While these assumptions simplify the computational complexity, they were carefully considered to ensure the validity and relevance of the study findings. The assumptions are as follows:

1) The reaction gases and their mixtures behave as ideal gases.
2) The interfaces between the components have excellent contact, and contact thermal resistance can be neglected.
3) The influence of gravity on component transport processes is negligible.

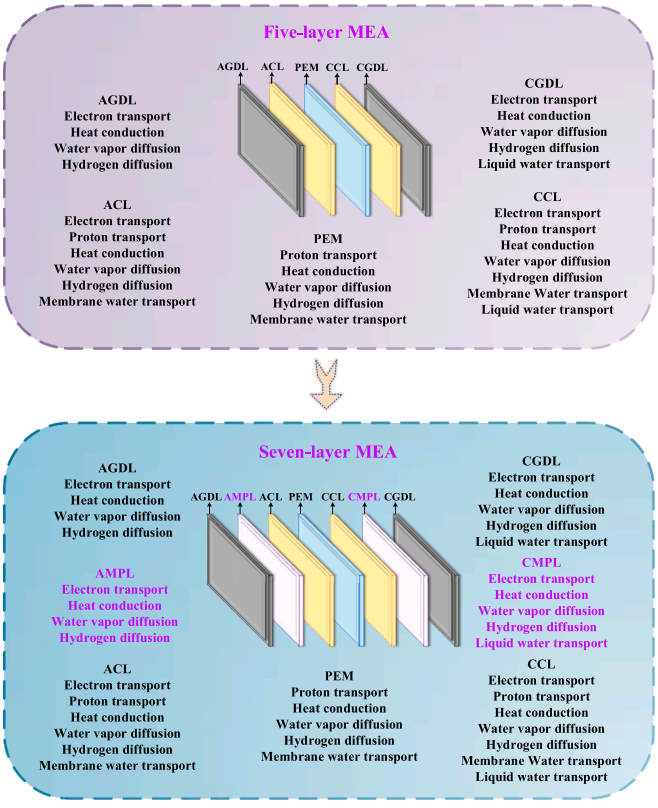

Fig. 1. Schematic of the MEA structure of a single PEMFC.

4) Gas convection and transmembrane transport of liquid water are negligible.

2.2. Model equations

This study focuses on a seven-layer MEA structure in PEMFC. To solve the numerical equations, a set of mathematical equations governing mass, momentum, energy, component, and electrochemical conservation was employed. Various parameters such as heat, potential, and gas content were calculated using fundamental laws. Fig. 2 shows the flowchart of the entire modelling process. The equations and their corresponding sources are summarised in Tables 1 and 2.

2.2.1. Mass conservation equation

During PEMFC operation, transport of H_2 and O_2 occurs within the cell. The mass conservation equation can be represented by Eq. (1):

$$\nabla\cdot\left(\varepsilon^{\mathrm{eff}}c_{\mathrm{m}}\overline{u}_{\mathrm{m}}\right)=S_{\mathrm{m}} \tag{1}$$

where, c_{m} denotes the concentration of the mixture, $\overline{u}_{\mathrm{m}}$ is the average mass flow rate of the mixture, S_{m} represents the mass source term, and $\varepsilon^{\mathrm{eff}}$ indicates the effective porosity, which is related to the volumetric porosity ε and liquid saturation s of the component material, as indicated in Eq. (2).

$$\varepsilon^{\mathrm{eff}}=\varepsilon(1-s) \tag{2}$$

In the mass conservation equation, the source term S_{m} represents the mass transfer associated with the consumption and generation of substances during electrochemical reaction processes, as well as the mass transfer related to phase transitions in the mass balance [19]. The hydrogen consumption, oxygen consumption, and water generation at the anode and cathode can be calculated by applying Faraday's law [20].

$$S_{\mathrm{F}}=\frac{i}{nF} \tag{3}$$

$$S_{\mathrm{m}}=S_{\mathrm{H_2}}+S_{\mathrm{O_2}}+S_{\mathrm{H_2O}}=\left(-\frac{i}{2F}M_{\mathrm{H_2}}-\frac{i}{4F}M_{\mathrm{O_2}}\right)+S_{\mathrm{H_2O}} \tag{4}$$

where, $S_{\mathrm{H_2}}$ is the consumption of hydrogen at the anode, $S_{\mathrm{O_2}}$ is the consumption of oxygen at the cathode, and $S_{\mathrm{H_2O}}$ represents the internal water content, which includes the mass transfer processes of absorption/desorption and evaporation/condensation.

2.2.2. Momentum conservation equation

$$\nabla\cdot\left(\frac{1}{\left(\varepsilon^{\mathrm{eff}}\right)^2}c_{\mathrm{m}}\overline{u}_{\mathrm{m}}\overline{u}_{\mathrm{m}}\right)=-\nabla p_{\mathrm{m}}+\nabla\cdot\left(\frac{1}{\varepsilon^{\mathrm{eff}}}\mu_{\mathrm{m}}\nabla\overline{u}_{\mathrm{m}}\right)+S_{\mathrm{u}} \tag{5}$$

where, p_{m} is the pressure, μ_{m} is the viscosity of the mixture, and S_{u} is the momentum source term.

The viscous resistance resulting from the interaction between the fluid and porous walls of the GDL and CL can be determined using Darcy's law [21]:

$$S_{\mathrm{u}}=-\left(\frac{\mu_{\mathrm{m}}\overline{u}_{\mathrm{m}}}{\kappa}\right) \tag{6}$$

where, κ represents the permeability of the porous medium.

The dynamic viscosity of water can be calculated using the Vogel equation [22] in the temperature range of 2—95 °C.

$$\mu_{\mathrm{m}}=\exp\left(-3.63148+\frac{542.05\mathrm{K}}{T-144.12\mathrm{K}}\right) \tag{7}$$

2.2.3. Energy conservation equation

The temperature distribution plays a critical role in component

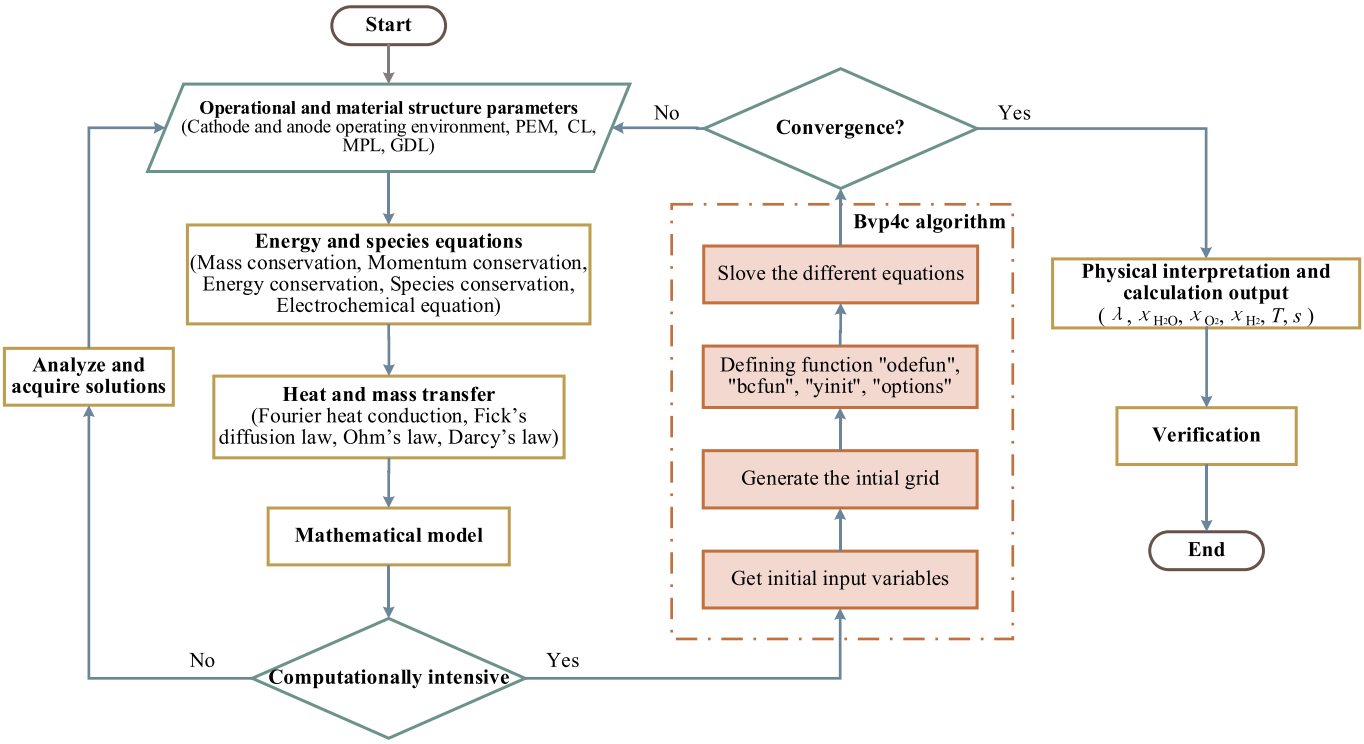

Fig. 2. Flowchart of the numerical solution method.

Table 1
Governing equations of the model.

Name	Dependent variable	Flux	Continuity equation
Ohm's law - electrons	ϕ_e	$j_e = -\sigma_e \nabla \phi_e$	$\nabla \cdot j_e = S_e$
Ohm's law - protons	ϕ_p	$j_p = -\sigma_p \nabla \phi_p$	$\nabla \cdot j_p = S_p$
Fourier heat conduction	T	$j_T = -k \nabla T$	$\nabla \cdot j_T = S_T$
Water transport in ionomer	λ	$j_\lambda = -(D_\lambda / V_m) \nabla \lambda + (\xi / F) j_p$	$\nabla \cdot j_\lambda = S_\lambda$
Darcy's law - liquid water	l	$j_l = -(\kappa / \mu \cdot V_w)(\partial p_c / \partial l) \nabla l$	$\nabla \cdot j_l = S_l$
Fick's diffusion law - water vapor	χ_{H_2O}	$j_{H_2O} = -cD_{H_2O} \nabla \chi_{H_2O}$	$\nabla \cdot j_{H_2O} = S_{H_2O}$
Fick's diffusion law - H_2	χ_{H_2}	$j_{H_2} = -cD_{H_2} \nabla \chi_{H_2}$	$\nabla \cdot j_{H_2} = S_{H_2}$
Fick's diffusion law - O_2	χ_{O_2}	$j_{O_2} = -cD_{O_2} \nabla \chi_{O_2}$	$\nabla \cdot j_{O_2} = S_{O_2}$

transport because of its intimate connection with the saturation pressure and temperature. The energy conservation equation is formulated as follows:

$$\nabla \cdot \sum_{k=l,g} \left(\varepsilon^{\text{eff}} S_k c_k h_k \overline{u_k} \right) = \nabla \cdot \left(k_{\text{eff}} \nabla T - \sum_i h_i j_i \right) + S_T \tag{8}$$

where, the terms on the right side represent the energy associated with the fluid flow and diffusion transport. k_{eff} is the effective heat conductivity of the porous medium (Eq. (9)), h_i represents the enthalpy of the component (Eq. (10)), j_i denotes the flux of the component, and S_T is the energy source term.

$$k_{\text{eff}} = \varepsilon^{\text{eff}} k_m + \left(1 - \varepsilon^{\text{eff}}\right) k_s \tag{9}$$

$$h_i = \int_{T_{\text{ref}}}^{T} C_{p,i} dT \tag{10}$$

where, T_{ref} is the reference temperature, whose value is 298.15 K.

In the species transport process, the phase transitions latent heat can be calculated by adding the following equations to the total heat source term:

$$\begin{aligned} S_{T,ad} &= h_{ad} S_{ad} \\ S_{T,ec} &= h_{ec} S_{ec} \end{aligned} \tag{11}$$

where, h_{ad} represents the molar enthalpy of the absorption or desorption process and h_{ec} is the molar enthalpy of the evaporation or condensation

Table 2
Source terms in the governing equations.

Source		S_e	S_p	S_T	S_λ	S_{H_2O}	S_{H_2}	S_{O_2}	S_l
AGDL	=	0		$S_{T,e}$		0	0		
AMPL	=	0		$S_{T,e}$		0	0		
ACL	=	$-i$	i	$S_{T,e} + S_{T,p} + S_{T,r} + S_{T,abs/des}$	$S_{abs/des}$	$-S_{abs/des}$	$-S_F$		
PEM	=		0	$S_{T,p}$	0				
CCL	=	i	$-i$	$S_{T,e} + S_{T,p} + S_{T,rea} + S_{T,abs/des} + S_{T,eva/con}$	$S_F + S_{abs/des}$	$-S_{abs/des} - S_{eva/con}$		$-S_F/2$	$S_{eva/con}$
CMPL	=	0		$S_{T,abs/des} + S_{T,eva/con}$		$-S_{eva/con}$		0	$S_{eva/con}$
CGDL	=	0		$S_{T,abs/des} + S_{T,eva/con}$		$-S_{eva/con}$		0	$S_{eva/con}$

process. The heat generated by protons and electrons can be calculated using Joule's first law:

$$\begin{aligned} S_{\mathrm{T,e}} &= -j_{\mathrm{e}}\cdot\nabla\phi_{\mathrm{e}} \\ S_{\mathrm{T,p}} &= -j_{\mathrm{p}}\cdot\nabla\phi_{\mathrm{p}} \end{aligned} \tag{12}$$

The heat generated by the electrochemical reactions can be divided into activation heat and Peltier heat. The total heat can be calculated using the following equation [23]:

$$S_{\mathrm{T,r}} = i\eta - S_{\mathrm{F}} \times \begin{cases} T\Delta S_{\mathrm{HOR}} \\ T\Delta S_{\mathrm{ORR}} \end{cases} \tag{13}$$

where, i is the current density, η is the activation overpotential, ΔS_{HOR} and ΔS_{ORR} are the entropy changes during hydrogen oxidation and oxygen reduction, respectively.

2.2.4. Species conservation equation

In the electrochemical reactions of PEMFCs, the component conservation equations for each gas can be expressed as follows:

$$\nabla\cdot\left(\varepsilon^{\mathrm{eff}} c_{\mathrm{m}}\overline{u_{\mathrm{m}}}\omega_{\mathrm{i}}\right) = \nabla\cdot\left(\varepsilon^{\mathrm{eff}}\rho_{\mathrm{m}} D_{\mathrm{i,m}}^{\mathrm{eff}}\nabla\omega_{\mathrm{i}}\right) + S_{\mathrm{i}} \tag{14}$$

where, ω_{i} represents the mass transfer coefficient of component i, $D_{\mathrm{i,m}}^{\mathrm{eff}}$ is the effective diffusion coefficient of component i, and S_{i} denotes the source term, including the oxygen consumption and water generation in the CL, as well as the phase change of the internal components.

For different gas components, the effective transport coefficient is calculated by

$$D_{\mathrm{i}} = \frac{\varepsilon}{\tau^2}(1-s)^3 D_{\mathrm{i}}^{\mathrm{ref}}\left(\frac{p_{\mathrm{ref}}}{p}\right)\left(\frac{T}{T_{\mathrm{ref}}}\right)^{1.5} \tag{15}$$

where, ε is the volume fraction of pores, τ is the tortuosity of pores, and $D_{\mathrm{i}}^{\mathrm{ref}}$ represents the reference diffusion coefficients for different components, with values of 0.36 (water vapour in air), 0.28 (oxygen in air), and 1.24 (water vapour in hydrogen).

2.2.5. Electrochemical equation

The conservation equations for electrons and protons can be expressed as follows:

$$\nabla\cdot(\sigma_{\mathrm{e}}\nabla\phi_{\mathrm{e}}) = S_{\phi_{\mathrm{e}}} \tag{16}$$

$$\nabla\cdot\left(\sigma_{\mathrm{p}}\nabla\phi_{\mathrm{p}}\right) = S_{\phi_{\mathrm{p}}} \tag{17}$$

where, ϕ_{e} and ϕ_{p} are the electrode and electrolyte potentials, respectively; and σ_{e} and σ_{p} are the electronic and proton conductivities, respectively.

The ion conductivity λ is determined using the percolation theory with Arrhenius temperature correction [24], and it can be calculated using the following formula:

$$\sigma_p = \varepsilon_{eff}^{1.5} 116\frac{s}{m}\max\{0, f-0.06\}^{1.5} \times \exp\left[\frac{15}{R}\left(\frac{1}{T_{ref}}-\frac{1}{T}\right)\right] \tag{18}$$

$$f = \frac{\lambda V_{\mathrm{m}}}{V_{\mathrm{m}} + \lambda V_{\mathrm{w}}} \tag{19}$$

where, $\varepsilon_{\mathrm{eff}}$ is the effective porosity of the polymer, f is the volume fraction of water in the polymer, V_{m} is the equivalent volume of the dry film (equivalent weight ratio to mass density), and V_{w} is the volume of membrane water.

The reversible cell voltage can be calculated using the Nernst equation [19]:

$$\Delta\phi_0 = -\frac{\Delta G}{2F} + \frac{RT}{2F}\ln\left[\left(\frac{p_{\mathrm{H_2}}}{p_{\mathrm{ref}}}\right)\left(\frac{p_{\mathrm{O_2}}}{p_{\mathrm{ref}}}\right)^{0.5}\right] \tag{20}$$

The reaction rate in the CL is calculated using the Butler-Volmer equation:

$$i = i_0 a\left[\exp\left(\frac{2\beta F}{RT}\eta\right) - \exp\left[-\frac{2(1-\beta)F}{RT}\eta\right]\right] \tag{21}$$

where, β represents the symmetry factor, F is Faraday's constant, and η denotes the activation overvoltage, whose calculation formula is

$$\eta = \begin{cases} \Delta\phi - \Delta\phi_0 \text{ in ACL} \\ \Delta\phi_0 - \Delta\phi \text{ in CCL} \end{cases} \tag{22}$$

where, $\Delta\phi$ is the Galvani potential difference between protons and electrons and $\Delta\phi_0$ represents the reversible potential difference, which can be calculated using the following equation:

$$\Delta\phi_0 = \begin{cases} -\dfrac{T\Delta S_{\mathrm{HOR}}}{2F} - \dfrac{RT}{2F}\ln\left(\dfrac{p_{\mathrm{H_2}}}{p_{\mathrm{ref}}}\right) \text{ in ACL} \\ -\dfrac{\Delta h - T\Delta S_{\mathrm{ORR}}}{2F} + \dfrac{RT}{4F}\ln\left(\dfrac{p_{\mathrm{O_2}}}{p_{\mathrm{ref}}}\right) \text{ in CCL} \end{cases} \tag{23}$$

2.2.6. Membrane water transport

The presence of water in the membrane phase significantly affects the ion conductivity of the PEM. The water transport in the PEM and CL can be described as follows:

$$\nabla\cdot(D_\lambda\nabla c_\lambda) - \nabla\cdot(2\xi S_{\mathrm{F}}) = S_\lambda \tag{24}$$

where, ξ is the electric dragging force, and D_λ is the diffusion coefficient of water in the film state, which is calculated as follows [20]:

$$D_\lambda = 2.1\times10^{-7}\exp\left(-\frac{2346}{T}\right)c_{\mathrm{w}} \tag{25}$$

The membrane water content is defined as the number of water molecules per sulfonic acid group in the polymer electrolyte and is related to the concentration of membrane water. The transport process is primarily influenced by the electric drag force.

$$\lambda = \frac{EW}{\rho_{\mathrm{m}}}c_\lambda \tag{26}$$

$$\xi = \frac{2.5\lambda}{22} \tag{27}$$

where, ρ_{m} is the density of the PEM, EW is the equivalent weight of the dry film, and c_λ is the membrane water concentration.

The equilibrium membrane water content λ_{eq} at steady state depends on the relative humidity [19], and the relationship is given by the following equation:

$$\lambda_{\mathrm{eq}} = 0.043 + 17.81RH - 39.85RH^2 + 36RH^3 \tag{28}$$

where, RH is the relative humidity of gas.

Owing to the absorption/desorption of water at the interface between the CL and PEM, the water uptake S_{ad} is primarily determined by the relationship between λ and λ_{eq} [25], as follows:

$$S_{\mathrm{ad}} = \begin{cases} \dfrac{\gamma_{\mathrm{abs}}\rho_{\mathrm{m}}}{EW}\left(\lambda_{\mathrm{eq}} - \lambda\right) \text{ if } \lambda < \lambda_{\mathrm{eq}} \\ \dfrac{\gamma_{\mathrm{des}}\rho_{\mathrm{m}}}{EW}\left(\lambda_{\mathrm{eq}} - \lambda\right) \text{ if } \lambda > \lambda_{\mathrm{eq}} \end{cases} \tag{29}$$

where, γ_{abs} and γ_{des} represent the absorption and desorption rate coefficients, respectively. Ge et al. [26] developed a formula for calculating the absorption and desorption rate coefficients of Nafion films:

$$\begin{cases} \gamma_{abs} = \dfrac{1.14\times10^{-5} f}{L_{CL}} \exp\left[2416\left(\dfrac{1}{T_{ref}} - \dfrac{1}{T}\right)\right] \\ \gamma_{des} = \dfrac{4.59\times10^{-5} f}{L_{CL}} \exp\left[2416\left(\dfrac{1}{T_{ref}} - \dfrac{1}{T}\right)\right] \end{cases} \tag{30}$$

where, L_{CL} is the thickness of the CL.

2.2.7. Liquid water transport

The conservation equation for liquid water is

$$\nabla\cdot\left(\varepsilon^{eff} v_l \rho_l \overline{u_m}\right) = \nabla\cdot(\rho_l D_l \nabla s) - S_l \tag{31}$$

where, ν_l, ρ_l, and D_l are the volume fraction, density, and diffusion coefficient (Eq. (32)) of liquid water, respectively, whereas S_l is the source term for liquid water.

$$D_l = -\frac{\kappa_l}{\eta}\frac{dp_c}{ds} \tag{32}$$

where, κ_l is the permeability coefficient of liquid water (Eq. (33)), and p_c is the capillary pressure (Eq. (34)) [27].

$$\kappa_l = \left(10^{-6} + s_{red}^3\right)\kappa_{abs} \tag{33}$$

$$p_c = -0.0011\exp[-44.02(s-0.496)\,] + 278.3\exp[8.103(s-0.496)\,] - 191.8 \tag{34}$$

In the above equations, the dependence of liquid water saturation at the phase change interface is introduced through a reduction in the saturation level [19]:

$$s_{red} = \frac{s - s_{im}}{1 - s_{im}} \tag{35}$$

When the partial pressure of water vapour exceeds the saturation pressure, liquid water is formed, and the equation is as follows:

$$S_{ec} = \begin{cases} \gamma_{eva} c\left(\chi_{H_2O} - \chi_{sat}\right) \text{ if } \chi_{H_2O} < \chi_{sat} \\ \gamma_{con} c\left(\chi_{H_2O} - \chi_{sat}\right) \text{ if } \chi_{H_2O} > \chi_{sat} \end{cases} \tag{36}$$

where, γ_{eva} and γ_{con} are the evaporation and condensation rate coefficients respectively, which are calculated using the following formulas [25]:

$$\begin{aligned} \gamma_{evp} &= K_{evp} a_{lg} s_{red} \\ \gamma_{con} &= K_{con} a_{lg} (1 - s_{red}) \end{aligned} \tag{37}$$

where, K_{evp} and K_{con} are the Hertz-Knudsen mass transfer coefficient, which can be obtained under atmospheric pressure [28]:

$$\left.\begin{matrix} K_{evp} \\ K_{con} \end{matrix}\right\} = \sqrt{\frac{RT}{2\pi M_l}} \times \begin{cases} 5\times10^{-4} \\ 6\times10^{-3} \end{cases} \tag{38}$$

where, M_l is the molar mass of water, whose value is 18 g/mol.

The water vapour saturation pressure p_{sat} as a function of the local temperature can be calculated using the following equation [21]:

$$p_{sat} = -2846.4 + 411.24\times(T - 273.15) - 10.554 \times (T-273.15)^2 + 0.16636\times(T-273.15)^3 \tag{39}$$

2.3. Boundary conditions

Humidification of the reactant gases occurs at the cathode and anode sides, and the water vapour content can be determined based on the relative humidity:

$$\begin{aligned} \chi_{H_2O}^{an} &= \frac{p_{sat}(T_{an}) RH_{an}}{P_{an}} \\ \chi_{H_2O}^{ca} &= \frac{p_{sat}(T_{ca}) RH_{ca}}{P_{ca}} \end{aligned} \tag{40}$$

In the PEMFC, the molar fraction χ_{H_2/O_2} of the reactant gas can be calculated based on the molar fraction of the dry reactant gas α and molar fraction χ_{H_2O} of water vapour.

$$\begin{aligned} \chi_{H_2} &= \alpha_{H_2}\left(1 - \chi_{H_2O}^{an}\right) \\ \chi_{O_2} &= \alpha_{H_2}\left(1 - \chi_{H_2O}^{ca}\right) \end{aligned} \tag{41}$$

According to Faraday's law, the following flux equations respectively describe the diffusion of hydrogen at the anode and oxygen at the cathode:

$$\begin{aligned} j_{H_2} &= \frac{i}{2F} \\ j_{O_2} &= \frac{i}{4F} \end{aligned} \tag{42}$$

At the GDL/gas channel (GC) interface, the temperature T and pressure p are governed by the Dirichlet conditions:

$$\begin{aligned} T &= T_{an/ca} \\ p &= p_{an/ca} \end{aligned} \tag{43}$$

2.4. Performance and operating parameters of membrane electrode assembly

The numerical model constructed in this study incorporates the essential structural parameters of the MEA components, such as the thickness, conductivity, thermal conductivity, porosity, and absolute permeability. Through a comprehensive review of the existing literature, the MPL structural parameters were summarized, as listed in Table 3. Based on the existing studies and results, we selected Nafion 211 and Toray TGP-H-060 as the PEM and GDL materials, respectively [29,30]. The detailed specifications of the structural parameters of the other MEA components are provided in Table 4. Additionally, Table 5 presents the fundamental operating parameters used in this model to simulate and calculate the performance of PEMFCs under various operating conditions.

3. Results and discussion

3.1. Model validation

To validate the accuracy of the numerical model used in this study, a comparison was made between the simulation results and experimental data from Zhang et al. [41], under identical fuel cell component performance and operating conditions. Fig. 3 shows the close agreement between the simulated current density - voltage (I - V) and current density - power density (I - P) curves and the corresponding experimental results, confirming the reliability of the model calculations.

To further validate and analyse the results, a root mean square error (RMSE) analysis was conducted using the experimental data. Considering the significant variations in current under different operating conditions, a normalized RMSE ($RMSE_{nor}$) analysis was employed [42].

Table 3
Structural parameters of the MPL [16,18,31–38].

Parameters	Symbol	Value	Unit
Thickness	L_{MPL}	5, 10, 20, 30, 40, 50	μm
Thermal conductivity	k	1	$W{\cdot}m^{-1}{\cdot}K^{-1}$
Electrical conductivity	σ	1000	$S{\cdot}m^{-1}$
Absolute permeability	κ_{abs}	10^{-12}, 2×10^{-12}, 10^{-13}, 2×10^{-13}, 2.5×10^{-13}	m^2
Pore volume fraction	ε_p	0.3, 0.4, 0.5, 0.6	–
Pore tortuosity	τ	1.83, 1.58, 1.41, 1.26	–

Table 4
Structural parameters of the MEA components [19,39,40].

Components	Parameters	Symbol	Value	Unit
Proton exchange membrane	Thickness	L_{PEM}	25	μm
	Thermal conductivity	k	0.3	$W·m^{-1}·K^{-1}$
	Membrane equivalent weight	EW	1.1	$kg·mol^{-1}$
	Membrane density	ρ_m	1980	$kg·m^{-3}$
Anode/cathode gas diffusion layer	Thickness	L_{GDL}	160	μm
	Thermal conductivity	k	1.6	$W·m^{-1}·K^{-1}$
	Electrical conductivity	σ	1250	$S·m^{-1}$
	Absolute permeability	κ_{abs}	6.15×10^{-12}	m^2
	Pore volume fraction	ε_p	0.76	–
	Pore tortuosity	τ^*	1.15	–
	Contact angle	θ	130	°
Anode/cathode catalyst layer	Thickness	L_{CL}	10	μm
	Thermal conductivity	k	0.27	$W·m^{-1}·K^{-1}$
	Electrical conductivity	σ	350	$S·m^{-1}$
	Absolute permeability	κ_{abs}	10^{-13}	m^2
	Pore volume fraction	ε_p	0.4	–
	Pore tortuosity	τ	1.58	–

* Pore tortuosity calculation formula:$\tau = \varepsilon_p^{-0.5}$

Table 5
Operating parameters used in the base case of the model [19].

Parameters	Symbol	Value	Unit
Relative humidity - cathode	RH_{ca}	0.9	–
Relative humidity - anode	RH_{an}	0.9	–
Temperature - cathode	T_{ca}	348.15	K
Temperature - anode	T_{an}	348.15	K
Gas pressure - cathode	p_{ca}	1.5	bar
Gas pressure - anode	p_{an}	1.5	bar
Pressure - surroundings	p_{con}	1	bar
Molar fraction in dry fuel gas - hydrogen	α_{H_2}	1	–
Molar fraction in dry fuel gas - oxygen	α_{O_2}	0.21	–
Molar mass of water	M_l	18×10^{-3}	$kg·mol^{-1}$
Hydrogen diffusion coefficient - water vapor (standard reference value)	$D_{H_2\text{-}H_2O,ref}$	1.24	$cm^2·s^{-1}$
Oxygen diffusion coefficient - air (standard reference value)	$D_{O_2\text{-}air,ref}$	0.28	$cm^2·s^{-1}$
Water vapor diffusion coefficient - hydrogen (standard reference value)	$D_{H_2O\text{-}H_2,ref}$	1.24	$cm^2·s^{-1}$
Water vapor diffusion coefficient - air (standard reference value)	$D_{H_2O\text{-}O_2,ref}$	0.36	$cm^2·s^{-1}$
Liquid saturation at the CGDL/CGC interface *	s_c	0.12	–

* Liquid saturation at interface:$p_c = 2\gamma\cos\theta/r$

For the error analysis, voltage and power density values at the same current density were selected during the simulation process. The calculated RMSE and $RMSE_{nor}$ values are presented in Table 6. The analysis reveals that the $RMSE_{nor}$ values for numerical simulation and experimental research under different temperatures (Case 1 and Case 2) are 6.3 % (I - V)/7.9 % (I - P) and 6.0 % (I - V)/9.2 % (I - P), respectively. These values fall well within the acceptable error range, indicating the high accuracy of the model in this study.

$$RMSE = \sqrt{\frac{\sum_{i=1}^{n}\left(I_{sim}(U_i) - I_{ref}(U_i)\right)^2}{n}} \tag{44}$$

$$RMSE_{nor} = \sqrt{\frac{\sum_{i=1}^{n}\left(1 - \frac{I_{sim}(U_i)}{I_{ref}(U_i)}\right)^2}{n}} \tag{45}$$

3.2. Impact analysis of microporous layer thickness on the performance of the membrane electrode assembly

The thickness of the MPL is a recognised key parameter affecting the performance of the MEA, as demonstrated by Antonacci [43], Aoyama [44], and Naito [45]. The impact of the MPL thickness within the range of 5 to 50 μm, while maintaining the operating conditions and other structural parameters constant, was analysed. Specifically, we examined the influence of the MPL thickness on the hydrogen transport at the anode, oxygen transport at the cathode, water vapour transport, and liquid water saturation at the cathode.

3.2.1. Influence of microporous layer thickness on *I - V* and *I - P* curves

The polarisation curve provides insights into the polarisation losses in PEMFCs, which can be attributed to the activation, ohmic, and concentration polarisations. In Fig. 4 (a), the voltage loss resulting from the reaction kinetics under low current density conditions is termed as activation loss, which is a crucial factor for achieving a positive net reaction rate. The activation loss tends to increase with increasing reaction rate. Ohm's law states that ohmic loss originates from the impedance encountered during proton and electron conduction, and it linearly increases with higher current densities. Notably, the concentration loss becomes significant under high current densities. Concentration polarisation arises owing to resistance in the reactant transport process, resulting in a discrepancy between the actual and theoretical reactant concentrations at the CL surface. Consequently, the thickness of the MPL primarily influences the transport of the reactant gases, resulting in variations in the concentration loss, whereas the activation and ohmic losses remain relatively unaffected.

Based on the I - V curve shown in Fig. 4, it is evident that the MPL thickness primarily affects the concentration polarisation region. As the reactants move from the flow field to the CL, a reduction in their concentration within the CL occurs, which is known as concentration loss. Increasing the thickness of the MPL increases the impedance to reactant transport, which cause more concentration loss. Under constant voltage operating conditions, as the thickness of the MPL layer decreases from 50 to 5 μm, the concentration polarisation loss exhibits a hysteresis phenomenon, which indicates improved PEMFC performance. As displayed in Fig. 4, the power density of the PEMFC shows, an increasing trend followed by a decrease with increasing current density, reaching a maximum power density point. As the MPL thickness decreases, the maximum power density of the PEMFC gradually increases, and the cell performance is improved.

3.2.2. Influence of microporous layer thickness on the molar fractions of H_2 and O_2

According to the analysis in the previous section, the MPL thickness affects the concentration polarisation loss, which is mainly determined by the gas concentration involved in the electrochemical reactions at the PEM/CL interface. Therefore, in this model, assuming constant operating conditions, the effects of the MPL thickness on the molar fractions of H_2 at the anode side and O_2 at the cathode side were quantitatively analysed at output voltages of 0.5 V and 0.7 V. Fig. 5 depicts the molar fraction of H_2 at the anode MPL/CL interface, which gradually decreases within the range of 5 to 50 μm the MPL thickness. The difference in the H_2 molar fraction between the anode GDL/MPL and the anode MPL/CL

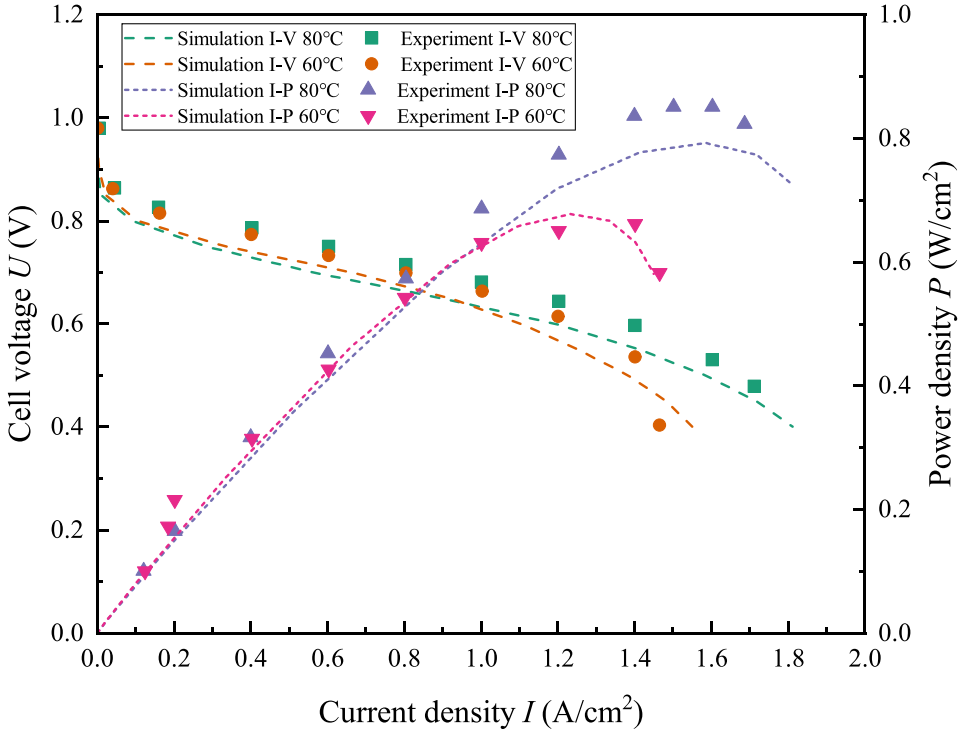

Fig. 3. Current density *I* - voltage *V* curve and current density *I* - power density *P* curve.

Table 6
Error analysis of simulation and experimental results.

Case	Temperature (℃)	Anode/ cathode relative humidity	Anode/ cathode pressure (kPa)		RMSE	$RMSE_{nor}$ (%)
1	80	0.92/0.92	50/50	I-V	0.043	6.3
				I-P	0.045	7.9
2	60	0.92/0.92	50/50	I-V	0.033	6.0
				I-P	0.031	9.2

interfaces positively correlates with the MPL thickness. Under the same output voltage, a larger difference in the H_2 molar fraction between the two interfaces indicates a higher transport resistance at the anode side. The H_2 molar fraction at the anode MPL/CL interface decreases from 0.763/0.765 to 0.760/0.763 (U = 0.5 V/0.7 V). Similarly, as shown in Fig. 6, the resistance of the mass transfer process at the cathode side gradually decreases with decreasing MPL thickness, resulting in a higher O_2 molar fraction being delivered to the cathode CL to participate in the electrochemical reaction. The O_2 molar fraction at the CCL/CMPL interface increases from 0.128/0.141 to 0.141/0.148 (U = 0.5 V/0.7 V).

Table 7 provides a comprehensive analysis of the difference in the gas molar fraction between the GDL/MPL and MPL/CL interfaces under varying current densities for MPL thicknesses of 5, 20, and 50 μm. According to Faraday's law, the consumption rates of hydrogen and oxygen are directly proportional to the current density, leading to increased reactant consumption at the PEM/CL interface under high power densities. A thicker MPL causes more resistance to the H_2 and O_2 transport processes, leading to a gradual increase in the difference in the gas molar fraction between the GDL/AMPL and MPL/CL interfaces. A thorough analysis of the gas molar fractions and their correlation with the MPL thickness enables a deeper understanding of the transport phenomena occurring within PEMFCs, particularly at the anode and cathode.

3.2.3. Influence of microporous layer thickness on the molar fraction of water vapour and liquid water saturation

From the data presented in Fig. 7, it is evident that the MPL thickness mainly affects the water vapour transport at the cathode side but not at the anode side. This is because of the migration of H^+ ions to the cathode CL interface, where they react with O_2 to generate water, resulting in a higher water content at the cathode side. The operating temperature and pressure conditions further contribute to water evaporation, which increases the water vapour content at the cathode side. As indicated in Table 8, there is a difference between the water vapour and liquid water saturation on the cathode side. Under MPL thickness conditions of 5 and 20 μm, the impact on water vapour transport remains relatively stable as voltage levels increase. This is due to the reduced impedance to water vapour transport at these thicknesses, which facilitates efficient diffusion. However, when the MPL thickness is increased to 50 μm, especially at a higher current density (U = 0.5 V), a significant increase in internal water generation within the cell occurs. Consequently, the pivotal role of the MPL thickness in enhancing water vapour diffusion becomes more pronounced, leading to a gradual increase in the concentration difference of water vapour between the GDL/MPL and the MPL/CL interfaces, particularly at the cathode side. As the MPL thickness increases from 5 to 50 μm, the resistance to water vapour transport increases, causing the water vapour content at the PEM/CCL interface to increase from 0.237/0.262 to 0.272/0.264 (U = 0.5 V/0.7 V), effectively preventing membrane dry-out during cell operation. Similarly, Fig. 8 displays comparable trends for liquid water transport and water vapour transport at the cathode side. As the MPL thickness increases, the liquid saturation of the CCL is enhanced, elevating the liquid water content at the PEM/CCL interface from 0.169/0.148 to 0.3/0.26 (U = 0.5 V/0.7 V).

The influence of MPL thickness on the transport of liquid water and water vapour can be attributed to two main factors. First, the progressive increase in MPL thickness from 5 to 50 μm gradually increases the resistance to water vapour and liquid water transport, leading to a higher water content at the PEM/CCL and the CCL/CMPL interfaces. These enhancements in the hydration state and conductivity of the membrane improve the MEA performance. Second, the increasing in

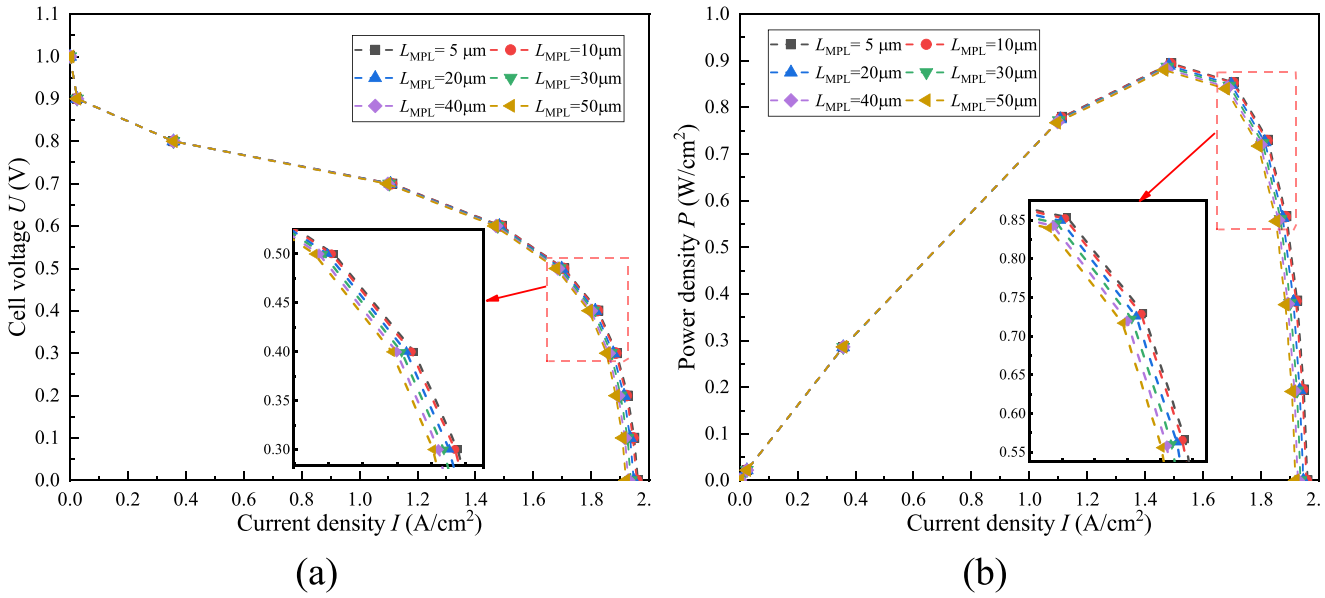

Fig. 4. Relationship curves under different MPL thicknesses: (a) I - V and (b) I - P.

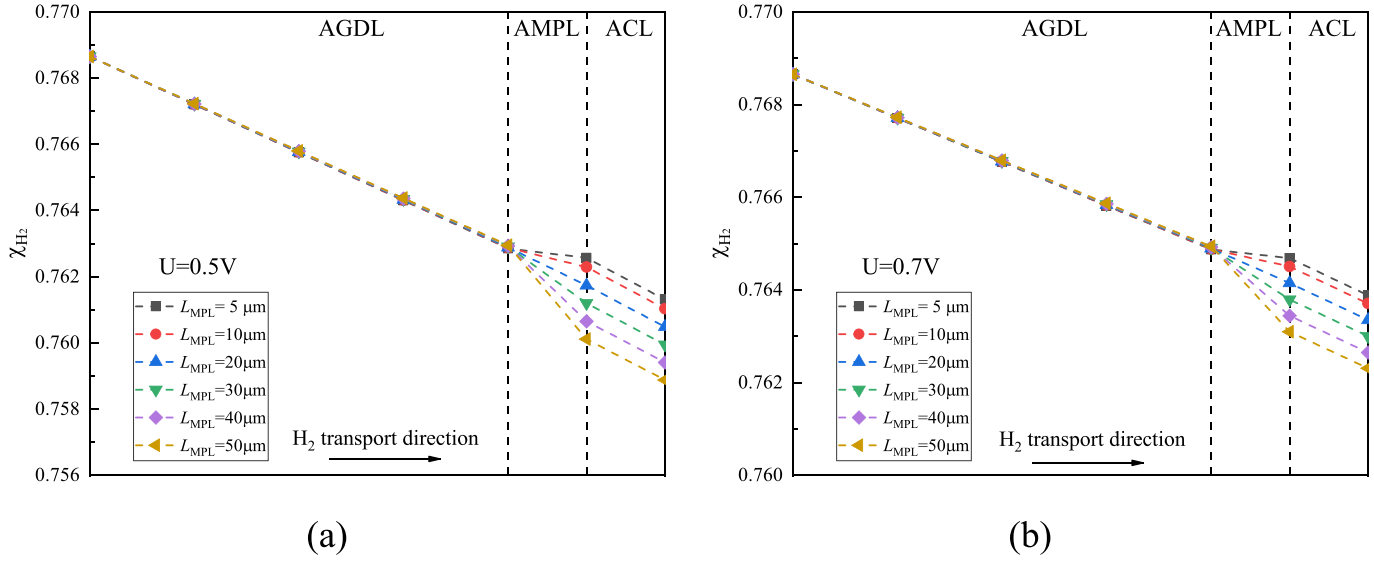

Fig. 5. Effect of MPL thickness on anode-side H_2 transport: (a) U = 0.5 V and (b) U = 0.7 V.

MPL thickness imposes a stronger hindrance on the transport of liquid water and water vapour. This causes pore blockage in the MPL, which obstructs oxygen transport and ultimately results in the performance degradation of PEMFCs. A comprehensive analysis of the water vapour and liquid water saturation dynamics provides crucial insights into the impact of the MPL thickness on water management, which plays a vital role in optimising the performance of PEMFCs.

3.2.4. Influence of microporous layer thickness on temperature distribution

Heat conduction is a fundamental heat transfer mechanism in fuel cell. In accordance with Fourier's law of heat conductivity, an increase in the thickness causes a corresponding shift in the heat transfer pathway and thermal resistance, giving rise to a substantial temperature gradient within the fuel cell. The relationship between the MPL thickness and internal temperature distribution at the output voltage of 0.5 V and 0.7 V is presented in Fig. 9. It can be observed that at the same output voltage, the temperature inside the PEM gradually increases as the MPL thickness increases. When the MPL thickness is constant, the temperature distribution inside the PEM exhibits a decreasing trend with an increase in voltage. At 0.5 V and 0.7 V, as the MPL thickness increases from 5 to 50 μm, its influence on heat transfer progressively intensifies, resulting in higher temperature distributions in the CL and PEM at the cathode side, with the highest temperatures of 349.54 K and 348.83 K, respectively. The elevated temperatures inside a fuel cell can decrease the liquid water fraction because water evaporates at high temperatures. Moreover, the elevated temperature increases the rate of diffusion of water vapour, which facilitates the transport of water vapour from the CCL and MPL to the GDL, thereby reducing the water content inside the fuel cell. Table 9 further reveals that, with the same MPL thickness, heat gradually accumulates inside the PEM as the output voltage decreases from 0.7 V to 0.5 V, resulting in an increase in the temperature difference between the cathode and anode sides of the PEM.

3.2.5. Summary and discussion

The findings reveal that reducing the MPL thickness significantly enhances the transport of the H_2 and O_2 reaction gases and reduces the

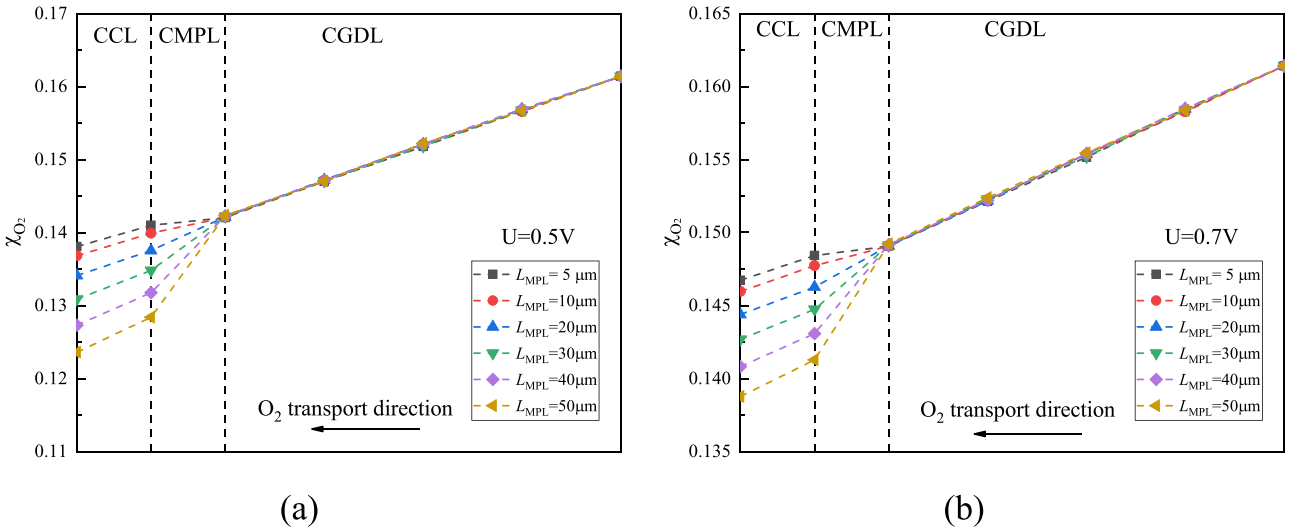

Fig. 6. Effect of MPL thickness on cathode-side O_2 transport: (a) U = 0.5 V and (b) U = 0.7 V.

Table 7
Difference in gas molar fractions between GDL/MPL and MPL/CL interfaces.

	Parameters	5 μm ($\times10^{-2}$)	20 μm ($\times10^{-2}$)	50 μm ($\times10^{-2}$)
$\Delta\chi_{H_2}$	0.5 V	0.03	0.11	0.28
	0.7 V	0.02	0.07	0.18
$\Delta\chi_{O_2}$	0.5 V	0.11	0.46	1.40
	0.7 V	0.07	0.28	0.80

volume and weight of the PEMFC, thus offering potential weight and size advantages. With respect to liquid water saturation, an increase in the MPL thickness improves the hydration condition of the CL while hindering gas transport. By contrast, reducing the MPL thickness improves the temperature distribution within the PEM and leads to a lower temperature gradient, which is favourable for internal heat transfer.

In the above analysis, when the MPL thickness is 5 μm, the fuel cell achieves optimal performance, as evidenced by its output power, gas transport and temperature distribution. Maintaining a certain MPL thickness is necessary to enhance the internal liquid water saturation and water vapour content, which in turn improves PEM conductivity. Proton transport within the PEM involves protons associated with water molecules that create hydrated hydrogen ions. These hydrated ions traverse the PEM, facilitating electrochemical reactions in the fuel cell. Concerning voltage losses in fuel cells, ohmic losses mainly result from the resistance during proton and electron transport. Notably, the water content and its distribution within the fuel cell substantially affect H^+ transport across the membrane, which influences ohmic losses. Therefore, to optimise PEMFC performance, it is essential to comprehensively analyse the effect of the MPL thickness on all relevant factors. This holistic perspective aids in determining the appropriate MPL thickness for

Table 8
Differences in water vapour and liquid water saturation at the GDL/MPL and MPL/CL interfaces.

	Parameters	5 μm ($\times10^{-2}$)	20 μm ($\times10^{-2}$)	50 μm ($\times10^{-2}$)
$\Delta\chi_{H_2O,ca}$	0.5 V	0.12	0.40	0.76
	0.7 V	0.13	0.40	0.47
Δs	0.5 V	2.15	6.60	15.46
	0.7 V	1.60	4.55	12.12

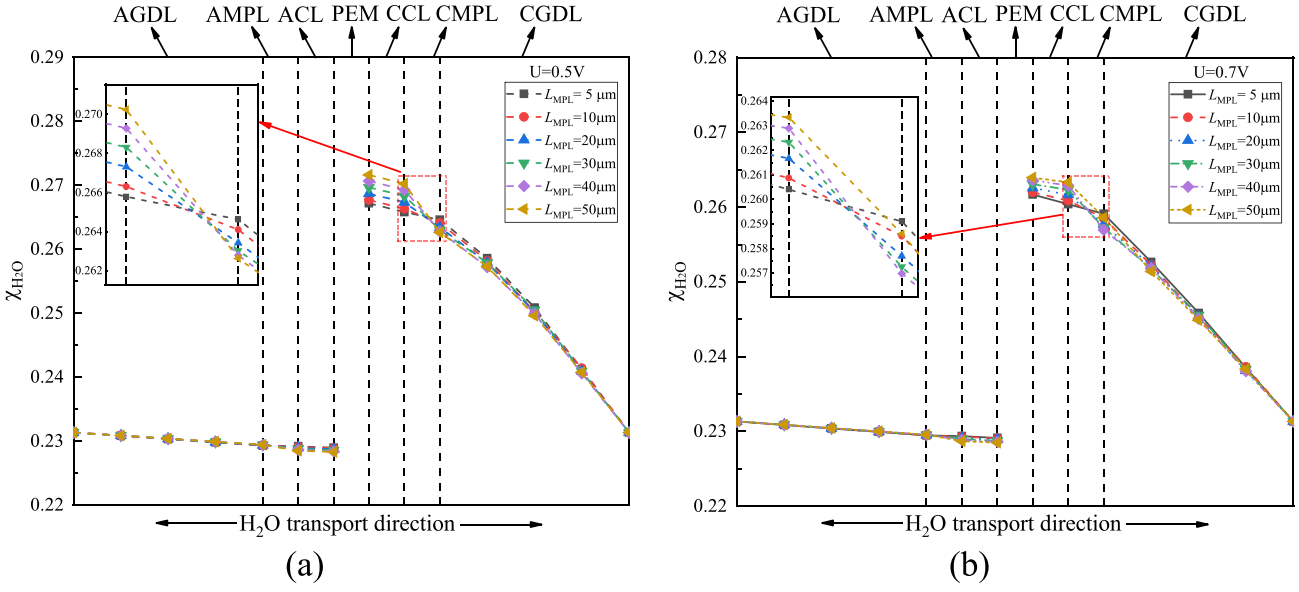

Fig. 7. Effect of MPL thickness on water vapour transport: (a) U = 0.5 V and (b) U = 0.7 V.

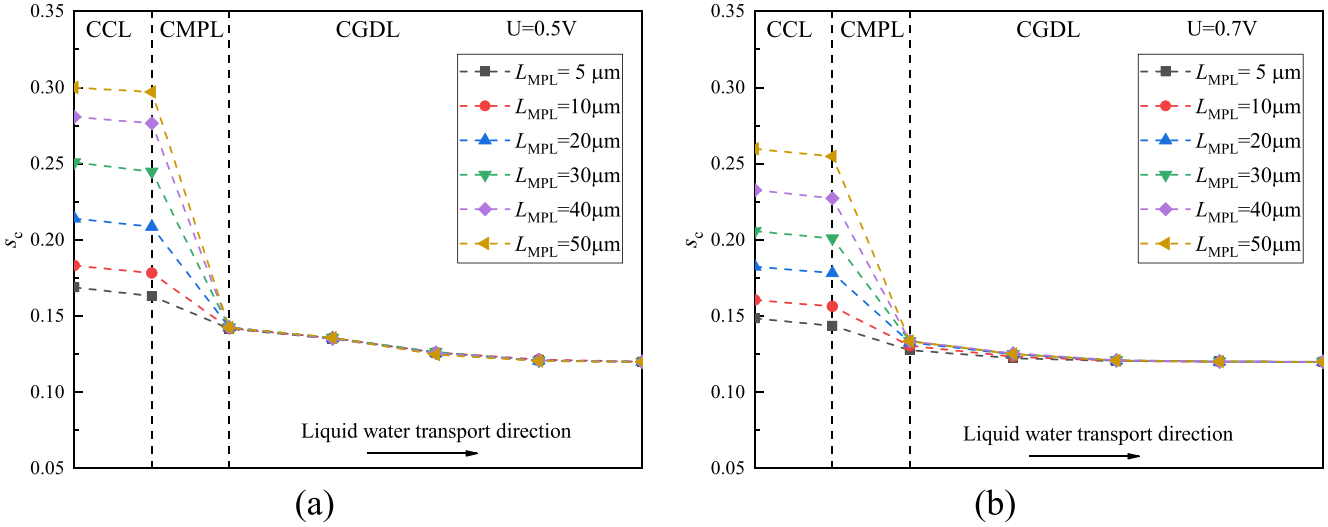

Fig. 8. Effect of MPL thickness on liquid water saturation: (a) U = 0.5 V and (b) U = 0.7 V.

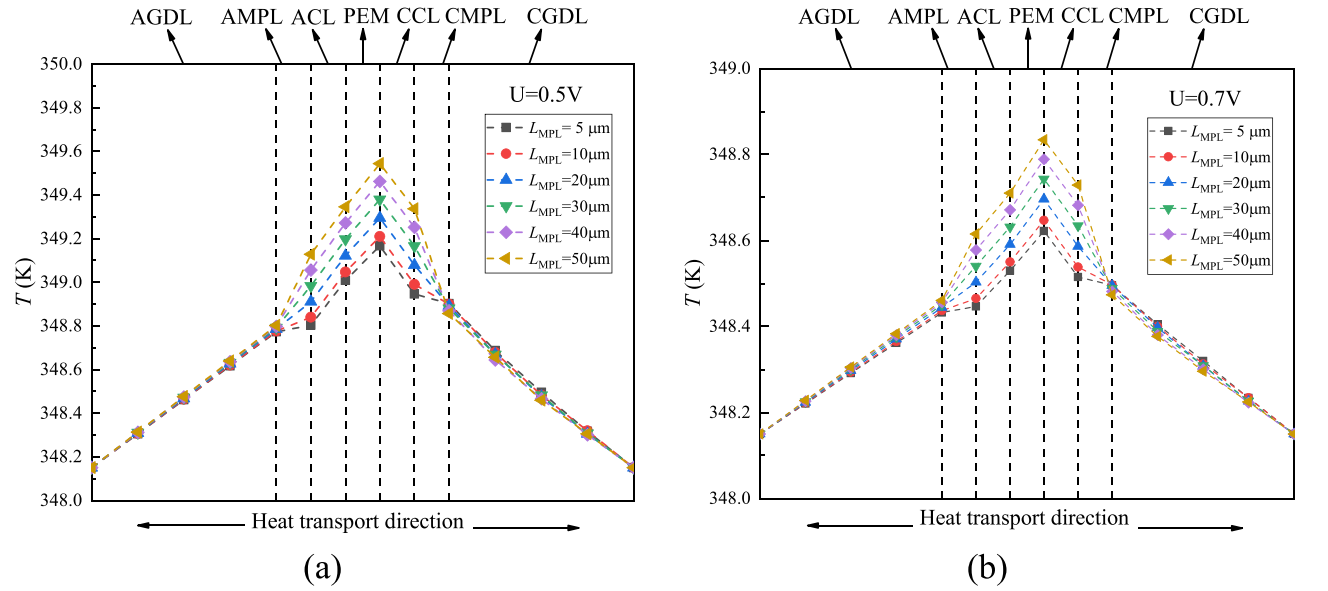

Fig. 9. Effect of MPL thickness on temperature distribution: (a) U = 0.5 V and (b) U = 0.7 V.

Table 9
Temperature difference between the two sides of the PEM.

	Parameters	5 μm ($\times 10^{-2}$)	20 μm ($\times 10^{-2}$)	50 μm ($\times 10^{-2}$)
ΔT	0.5 V	15.86	17.34	19.79
	0.7 V	9.21	10.47	12.36

maximising the PEMFC performance.

3.3. Influence of microporous layer porosity and absolute permeability on the performance of the membrane electrode assembly

Porosity and absolute permeability are crucial factors in evaluating the performance of porous media. Porosity represents the proportion of void spaces within a porous medium. In contrast, permeability quantifies the porous medium's capacity for fluid transmission, reflecting the level of ease with which fluids can move through it. Generally, a direct relationship exists between the porosity and permeability, wherein an increase in porosity corresponds to an increase in permeability. This is because a higher porosity provides additional pore volume for fluid flow, thereby facilitating the passage of fluid through a porous medium. The MPL thickness and the pore size and its distribution, jointly influence the heat and mass transfer. The pore size and its distribution are intricately linked to the porosity and permeability of the MPL. Thus, to consolidate the effects of these various factors, this study focused on the impacts of MPL porosity and permeability on gas and heat transfer.

Based on the preceding analysis of MPL thickness and its impact on the heat and mass transfer processes, we selected an MPL thickness of 5 μm and set different ranges of porosity, absolute permeability, and electrical conductivity (Table 4). The influences of porosity and absolute permeability on the molar fractions of H_2 at the anode side, O_2 at the cathode side, and levels of water vapour and liquid water saturation at the cathode side were analysed using a simulation program.

3.3.1. Influence of microporous layer porosity on the molar fractions of H_2 and O_2

Fig. 10 illustrates the impact of the porosity of the AMPL porosity on H_2 transport. The graph indicates that, under the same output voltage

conditions, increasing the MPL porosity from 0.3 to 0.6 leads to an increased number of channels for H_2 diffusion from the AGDL/AMPL interface to the AMPL/ACL interface. Consequently, the H_2 molar fraction at the AMPL/ACL interface gradually increases, thereby enhancing the diffusion transport of H_2 at the anode side. Additionally, Fig. 10 (a) and 10 (b) show that, with the same porosity, the current density of the fuel cell progressively increases as the output voltage decreases from 0.7 V to 0.5 V. This leads to an electrochemical reaction and a corresponding decrease in the H_2 molar fraction at the ACL/PEM interface by approximately 0.3 % in both cases.

The porosity of the CMPL has a comparable effect on the O_2 transport, as depicted in Fig. 11. At output voltages of 0.5 V and 0.7 V, an increase in porosity from 0.3 to 0.6 results in a 0.33 % and 0.21 % increase in the O_2 molar fraction at the CMPL/CCL interface, respectively. This increase enhances the O_2 molar fraction participating in the electrochemical reaction and accelerates the rate of electrochemical reactions at the cathode side. Therefore, increasing the porosity improves the operational characteristics of PEMFCs, particularly under high current densities. However, it should be noted that while a higher porosity improves the diffusion transport of H_2 at the anode side and O_2 at the cathode side, it also increases the presence of liquid water, which negatively affects the transport of reactant gases. The influence of porosity on the distribution of water vapour and liquid water is analysed in detail in Section 3.3.2.

3.3.2. *Influence of microporous layer porosity on the molar fraction of water vapour and liquid water saturation*

To further investigate the impact of MPL porosity on the MEA performance, the distributions of water vapour and liquid water within the MEA at output voltages of 0.5 V and 0.7 V were analysed, as depicted in Figs. 12 and 13. Fig. 12 shows that the MPL porosity mainly affects the water vapour transport at the cathode side, but not at the anode side. The difference in the water vapour molar fraction at the CCL/CMPL and CMPL/CGDL interfaces decreases with increasing porosity, which is mainly due to the enhancement of the water vapour transport path.

Furthermore, as indicated in Fig. 13, when the porosity is 0.6, increasing the output voltage from 0.5 V to 0.7 V results in a 2.04 % increase in liquid water saturation at the PEM/CCL interface. This can be attributed to the higher output voltage, which increases the power density and accelerates the electrochemical reaction rate within the fuel cell, consequently increasing the water generation. When the MPL porosity increases from 0.3 to 0.6 at U = 0.7 V, liquid water gradually diffuses from the CCL/CMPL interface towards the CMPL, causing the liquid water saturation to decrease from 15.48 % to 14.35 %, as displayed in Fig. 13 (b). This effectively mitigates the occurrence of cathode-side flooding. At a porosity level of 0.6, the MPL effectively enhances the transport of both water vapour and liquid water. However, it is essential to note that a higher porosity also means that more water can occupy the pores of the porous medium, thereby reducing the diffusion channels for O_2 at the cathode side and impeding the transport of reaction gas.

3.3.3. *Influence of microporous layer absolute permeability on the saturation of liquid water*

The permeability of a porous medium reflects its ability to transport liquids. Fig. 14 depicts the distribution of liquid water saturation at the cathode side of the fuel cell under different values of MPL absolute permeability. It can be observed from Fig. 14 (a) and 14 (b) that at output voltages of 0.5 V and 0.7 V, a decrease in MPL absolute permeability from 2×10^{-12} to 1×10^{-13} leads to an increase in liquid water saturation by 1.49 % and 0.74 %, respectively, at the PEM/CCL interface, indicating a hindered transport of internal liquid water. When the MPL permeability is 2×10^{-12} and the output voltage increases from 0.5 V to 0.7 V, the fuel cell's power density rises, resulting in increased water generation within the cell. As a result, the liquid water saturation at the PEM/CCL interface increases by 1.28 %. Comprehensive analysis of the above, the reduction in liquid water saturation at the PEM/CCL interface is attributed to the increased absolute permeability of the MPL, which diminishes the resistance of liquid water to flow through the pores of the porous medium and enhances the ability of the MPL to transport liquid water.

3.3.4. *Summary and discussion*

In this section, it is found that an increase in MPL porosity was found to have two significant effects. First, it enhances gas transport by increasing the number of additional channels for gas diffusion, particularly as the porosity increases from 0.3 to 0.6. This enhancement in gas transmission capability is beneficial for promoting reactant gas transport to the CL, leading to improved electrochemical reactions and higher fuel cell efficiency. However, a delicate balance must be achieved because a higher porosity also results in increased water occupancy within the pores. This can lead to a reduction in gas transport channels, potentially hindering reactant gas transport and affecting the fuel cell performance. Therefore, researchers should consider the trade-offs between enhanced gas transport and potential limitations in water management when optimising MPL porosity for specific fuel cell applications.

Additionally, our study highlights the significant role of the MPL absolute permeability in influencing liquid water saturation at the PEM/CCL interface. As the absolute permeability increases, the liquid water

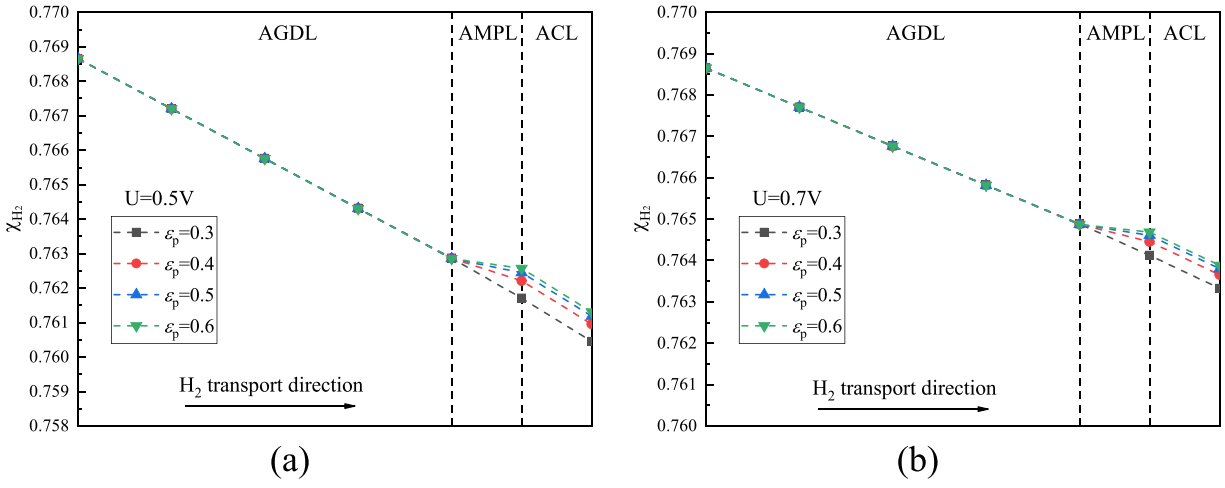

Fig. 10. Effect of MPL porosity on the distribution of H_2: (a) U = 0.5 V and (b) U = 0.7 V.

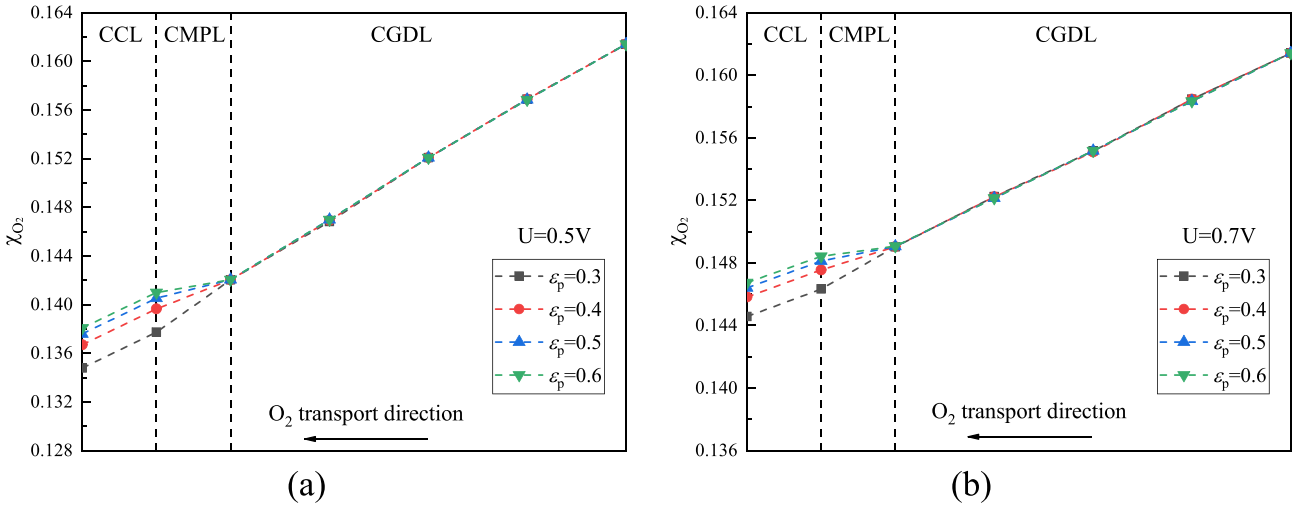

Fig. 11. Effect of MPL porosity on the distribution of O_2: (a) U = 0.5 V and (b) U = 0.7 V.

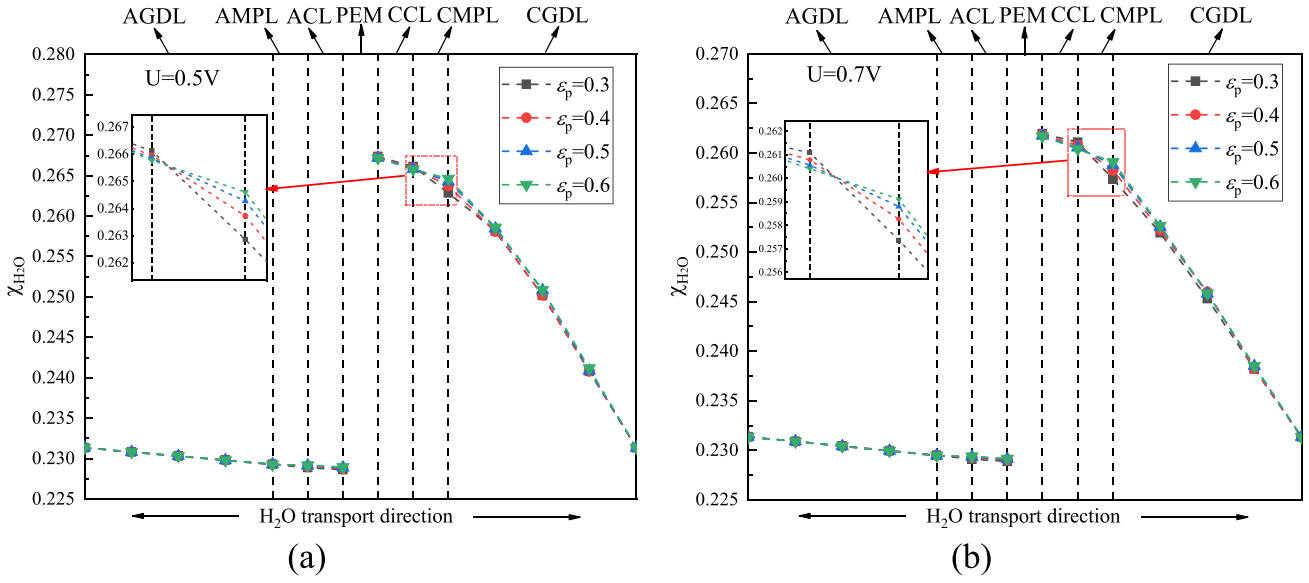

Fig. 12. Effect of MPL porosity on the distribution of water vapour: (a) U = 0.5 V and (b) U = 0.7 V.

saturation substantially decreases. This effect is critical for efficient water management in fuel cells, as it facilitates the removal of internal liquid water, which ultimately improves the overall durability and efficiency of PEMFCs.

4. Conclusions and future studies

This study focused on a comprehensive simulation and analysis of the impact of microporous layer parameters on the performance of membrane electrode assembly in fuel cell. Using a one-dimensional, two-phase, steady-state, non-isothermal model, we investigated the effects of the microporous layer thickness, porosity, and absolute permeability on various crucial aspects of fuel cell performance, including gas and water transport, temperature distribution, and liquid water saturation. By conducting a thorough analysis of the heat and mass transfer processes occurring within the membrane electrode assembly, the numerical simulation results provide invaluable insights into the substantial influence exerted by the microporous layer parameters on these transport processes. These findings highlight the pivotal role of microporous layer parameters in determining the overall performance of fuel cell, thus making a significant contribution to the advancement and broader adoption of fuel cell technology. The key findings and contributions of this study are outlined as follows:

1) The microporous layers considerably enhances water management in fuel cells. Reducing the microporous layer thickness from 50 to 5 μm remarkably improves the reactant transport in the membrane electrode assembly. Nevertheless, to comprehensively optimise the microporous layer thickness, it is necessary to adopt a multifaceted approach that considers the processing techniques, water content, and parametric interactions.
2) Increasing the microporous layer porosity improves the diffusion transport of H_2 at the anode side and O_2 at the cathode side. In terms of water transport, increasing the porosity from 0.3 to 0.6 reduces the liquid water saturation at the cathode catalyst layer and microporous layer interface by 0.52 % (U = 0.5 V) and 1.12 % (U = 0.7 V), thereby facilitating more efficient internal water transport.
3) Liquid water saturation in the fuel cell is significantly influenced by the permeability of the microporous layer. As the microporous layer permeability decreases from 2×10^{-12} to 1×10^{-13}, the liquid water

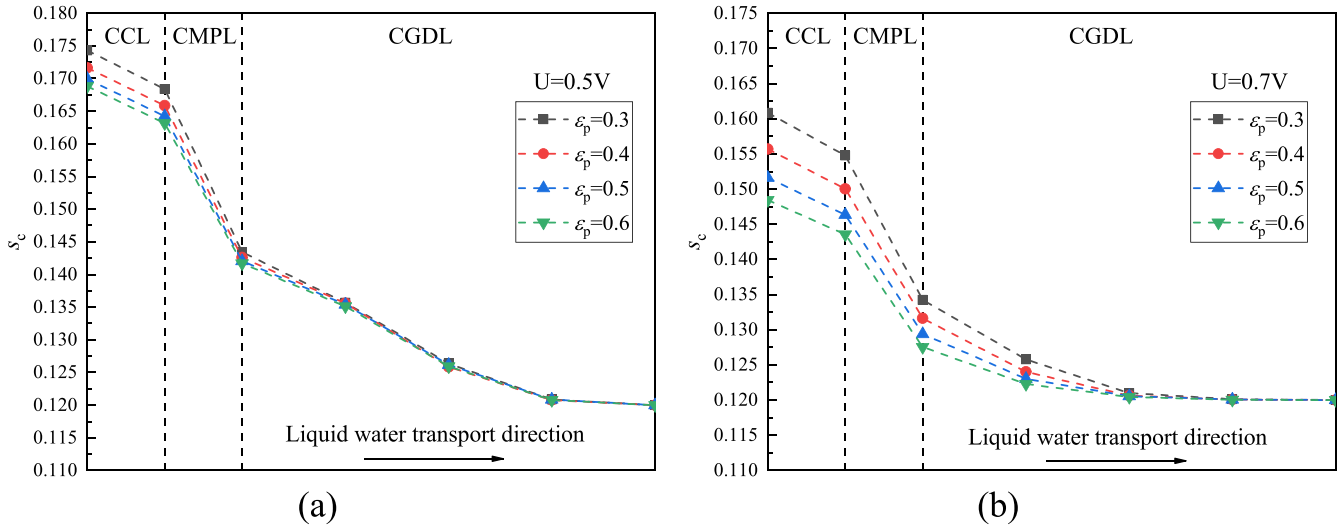

Fig. 13. Effect of MPL porosity on liquid water saturation: (a) U = 0.5 V and (b) U = 0.7 V.

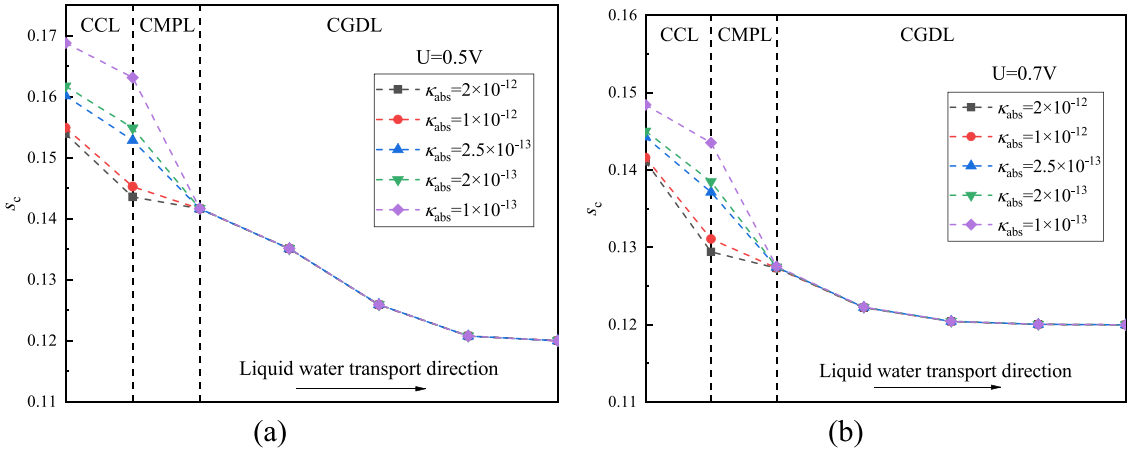

Fig. 14. Effect of MPL absolute permeability on liquid water saturation: (a) U = 0.5 V and (b) U = 0.7 V.

saturation at the proton exchange membrane and cathode catalyst layer interface increases by 1.49 % (U = 0.5 V) and 0.74 % (U = 0.7 V). This underscores the vital role of microporous layer permeability in enhancing internal liquid water removal and fuel cell water management.

The insights obtained from this study have significant implications for enhancing the efficiency of fuel cells and expanding their applications. For future research, several promising directions are proposed:

1) Exploring innovative microporous layer materials with tailored porosity and permeability has the potential to enhance fuel cell performance by mitigating trade-offs between gas and water transport and optimizing efficiency and durability.
2) Further research into microporous layer design and engineering can address the challenge of maintaining hydration while optimising reactant transport, enhancing performance across various conditions.
3) An enhanced comprehension of moisture transport at dielectric material interfaces, coupled with a detailed analysis of interfacial evaporation kinetics can improve the understanding and evaluation of the internal operating conditions of fuel cells.
4) Extending the model to two-dimensional and transient conditions can provide insights into the dynamic characteristics of fuel cells, enhancing the understanding of the effects of microporous layer parameters during start-up, shut-down, and load changes. This can lead to more robust and versatile fuel cell designs.

Declaration of Competing Interest

The authors declare that they have no known competing financial interests or personal relationships that could have appeared to influence the work reported in this paper.

Data availability

Data will be made available on request.

Acknowledgements

This work was supported by the Doctoral Scientific Research Foundation of Zhengzhou University of Light Industry (Grant No. 2020BSJJ082) .

References

[1] L. Zhou, Y. Zhou, Study on thermo-electric-hydrogen conversion mechanisms and synergistic operation on hydrogen fuel cell and electrochemical battery in energy

flexible buildings, Energ. Convers. Manage. 277 (2023) 116610, https://doi.org/10.1016/j.enconman.2022.116610.
[2] Y. He, Y. Zhou, Z. Wang, J. Liu, Z. Liu, G. Zhang, Quantification on fuel cell degradation and techno-economic analysis of a hydrogen-based grid-interactive residential energy sharing network with fuel-cell-powered vehicles, Appl. Energ. 303 (2021) 117444, https://doi.org/10.1016/j.apenergy.2021.117444.
[3] W. Song, H. Yu, Z. Shao, B. Yi, J. Lin, N. Liu, Effect of polytetrafluoroethylene distribution in the gas diffusion layer on water flooding in proton exchange membrane fuel cells, Chinese, J. Catal. 35 (2014) 468–473, https://doi.org/10.1016/S1872-2067(14)60014-0.
[4] K. Charoen, C. Prapainainar, P. Sureeyatanapas, T. Suwannaphisit, K. Wongamornpitak, P. Kongkachuichay, S.M. Holmes, P. Prapainainar, Application of response surface methodology to optimize direct alcohol fuel cell power density for greener energy production, J. Clean. Prod. 142 (2017) 1309–1320, https://doi.org/10.1016/j.jclepro.2016.09.059.
[5] Y. Luo, K. Jiao, Cold start of proton exchange membrane fuel cell, Prog. Energ. Combust. 64 (2018) 29–61, https://doi.org/10.1016/j.pecs.2017.10.003.
[6] E. Pahon, D. Bouquain, D. Hissel, A. Rouet, C. Vacquier, Performance analysis of proton exchange membrane fuel cell in automotive applications, J. Power Sources. 510 (2021) 230385, https://doi.org/10.1016/j.jpowsour.2021.230385.
[7] S. Shahgaldi, I. Alaefour, X. Li, Impact of manufacturing processes on proton exchange membrane fuel cell performance, Appl. Energ. 225 (2018) 1022–1032, https://doi.org/10.1016/j.apenergy.2018.05.086.
[8] M. Breitwieser, M. Klingele, S. Vierrath, R. Zengerle, S. Thiele, Tailoring the membrane-electrode interface in PEM fuel cells: A review and perspective on novel engineering approaches, Adv. Energy Mater. 8 (2018) 1701257, https://doi.org/10.1002/aenm.201701257.
[9] Z. Shangguan, B. Li, P. Ming, C. Zhang, Understanding the functions and modifications of interfaces in membrane electrode assemblies of proton exchange membrane fuel cells, J. Mater. Chem. a. 9 (2021) 15111–15139, https://doi.org/10.1039/D1TA01591E.
[10] A.Z. Weber, J. Newman, Effects of microporous layers in polymer electrolyte fuel cells, J. Electrochem. Soc. 152 (2005) A677, https://doi.org/10.1149/1.1861194.
[11] M. Blanco, D.P. Wilkinson, Investigation of the effect of microporous layers on water management in a proton exchange membrane fuel cell using novel diagnostic methods, Int. J. Hydrogen Energ. 39 (2014) 16390–16404, https://doi.org/10.1016/j.ijhydene.2014.07.147.
[12] K. Karan, H. Atiyeh, A. Phoenix, E. Halliop, J. Pharoah, B. Peppley, An experimental investigation of water transport in PEMFCs: The role of microporous layers, Electrochem. Solid St. 10 (2006) B34, https://doi.org/10.1149/1.2398728.
[13] H.K. Atiyeh, K. Karan, B. Peppley, A. Phoenix, E. Halliop, J. Pharoah, Experimental investigation of the role of a microporous layer on the water transport and performance of a PEM fuel cell, J. Power Sources. 171 (2007) 111–121, https://doi.org/10.1016/j.jpowsour.2007.04.016.
[14] J. Zhang, B. Wang, J. Jin, S. Yang, G. Li, A review of the microporous layer in proton exchange membrane fuel cells: Materials and structural designs based on water transport mechanism, Renew. Sust. Energ. Rev. 156 (2022) 111998, https://doi.org/10.1016/j.rser.2021.111998.
[15] P.H. Affonso Nóbrega, A review of physics-based low-temperature proton-exchange membrane fuel cell models for system-level water and thermal management studies, J. Power Sources. 558 (2023) 232585, https://doi.org/10.1016/j.jpowsour.2022.232585.
[16] Y. Li, Z. Zhou, X. Liu, W.-T. Wu, Modeling of PEM fuel cell with thin MEA under low humidity operating condition, Appl. Energy. 242 (2019) 1513–1527, https://doi.org/10.1016/j.apenergy.2019.03.189.
[17] L. Zuo, Q. Jian, Y. Yang, Durability improvement mechanism of proton exchange membrane fuel cell by microporous layer, Int. J. Energ. Res. 46 (2022) 18809–18818, https://doi.org/10.1002/er.8499.
[18] J. Zhou, S. Shukla, A. Putz, M. Secanell, Analysis of the role of the microporous layer in improving polymer electrolyte fuel cell performance, Electrochim. Acta. 268 (2018) 366–382, https://doi.org/10.1016/j.electacta.2018.02.100.
[19] R. Vetter, J.O. Schumacher, Free open reference implementation of a two-phase PEM fuel cell model, Comput. Phys. Commun. 234 (2019) 223–234, https://doi.org/10.1016/j.cpc.2018.07.023.
[20] T.E. Springer, T.A. Zawodzinski, S. Gottesfeld, Polymer electrolyte fuel cell model, J. Electrochem. Soc. 138 (1991) 2334, https://doi.org/10.1149/1.2085971.
[21] I. khazaee, H. Sabadbafan, Effect of humidity content and direction of the flow of reactant gases on water management in the 4-serpentine and 1-serpentine flow channel in a PEM (proton exchange membrane) fuel cell, Energy 101 (2016) 252–265, https://doi.org/10.1016/j.energy.2016.02.026.
[22] E. Jr, D.T. Goletz, An Antoine type equation for liquid viscosity dependency to temperature, Ind. Eng. Chem. Proc. Des. Dev. 16 (1977) 75–79, https://doi.org/10.1021/i260061a012.
[23] A.Z. Weber, R.L. Borup, R.M. Darling, P.K. Das, T.J. Dursch, W. Gu, D. Harvey, A. Kusoglu, S. Litster, M.M. Mench, R. Mukundan, J.P. Owejan, J.G. Pharoah, M. Secanell, I.V. Zenyuk, A critical review of modeling transport phenomena in polymer-electrolyte fuel cells, J. Electrochem. Soc. 161 (2014) F1254, https://doi.org/10.1149/2.0751412jes.
[24] A.Z. Weber, J. Newman, Transport in polymer-electrolyte membranes: II. Mathematical model, J. Electrochem. Soc. 151 (2004) A311, https://doi.org/10.1149/1.1639157.
[25] H. Wu, Mathematical modeling of transient transport phenomena in PEM fuel cells, University of Waterloo, 2009. Doctoral Thesis.
[26] S. Ge, X. Li, B. Yi, I.-M. Hsing, Absorption, desorption, and transport of water in polymer electrolyte membranes for fuel cells, J. Electrochem. Soc. 152 (2005) A1149, https://doi.org/10.1149/1.1899263.
[27] T.V. Nguyen, G. Lin, H. Ohn, X. Wang, Measurement of capillary pressure property of gas diffusion media used in proton exchange membrane fuel cells, Electrochem. Solid St. 11 (2008) B127, https://doi.org/10.1149/1.2929063.
[28] R. Marek, J. Straub, Analysis of the evaporation coefficient and the condensation coefficient of water, Int. J. Heat Mass Tran. 44 (2001) 39–53, https://doi.org/10.1016/S0017-9310(00)00086-7.
[29] J. Peron, A. Mani, X. Zhao, et al., Properties of Nafion® NR-211 membranes for PEMFCs, J Membrane Sci. 356 (2010) 44–51, https://doi.org/10.1016/j.memsci.2010.03.025.
[30] O.S. Burheim, J.G. Pharoah, H. Lampert, P.J.S. Vie, S. Kjelstrup, Through-plane thermal conductivity of PEMFC porous transport layers, ASME. J. Fuel Cell Sci. Technol. 8 (2011) 021013, https://doi.org/10.1115/1.4002403.
[31] X. Wang, T.V. Nguyen, Modeling the effects of the microporous layer on the net water transport rate across the membrane in a PEM fuel cell, J. Electrochem. Soc. 157 (2010) B496, https://doi.org/10.1149/1.3292287.
[32] L. Fan, G. Zhang, K. Jiao, Characteristics of PEMFC operating at high current density with low external humidification, Energ. Convers Manage. 150 (2017) 763–774, https://doi.org/10.1016/j.enconman.2017.08.034.
[33] P.Z. Lin, J. Sun, M.C. Wu, T.S. Zhao, A multiscale model for proton exchange membrane fuel cells with order-structured catalyst layers, Int. J. Heat Mass Tran. 195 (2022) 123092, https://doi.org/10.1016/j.enconman.2017.08.034.
[34] H. Meng, Multi-dimensional liquid water transport in the cathode of a PEM fuel cell with consideration of the micro-porous layer (MPL), Int. J. Hydrogen Energ. 34 (2009) 5488–5497, https://doi.org/10.1016/j.ijhydene.2009.04.067.
[35] X. Zhang, J. Yang, X. Ma, W. Zhuge, S. Shuai, Modelling and analysis on effects of penetration of microporous layer into gas diffusion layer in PEM fuel cells: Focusing on mass transport, Energy 254 (2022) 124103, https://doi.org/10.1016/j.energy.2022.124103.
[36] M. Andisheh-Tadbir, F.P. Orfino, E. Kjeang, Three-dimensional phase segregation of micro-porous layers for fuel cells by nano-scale X-ray computed tomography, J. Power Sources. 310 (2016) 61–69, https://doi.org/10.1016/j.jpowsour.2016.02.001.
[37] F. Salimi Nanadegani, E. Nemati Lay, B. Sunden, Computational analysis of the impact of a micro porous layer (MPL) on the characteristics of a high temperature PEMFC, Electrochim. Acta. 333 (2020) 135552, https://doi.org/10.1016/j.electacta.2019.135552.
[38] G. Zhang, A 3D model of PEMFC considering detailed multiphase flow and anisotropic transport properties, Int. J. Heat Mass Tran. 115 (2017) 714–724, https://doi.org/10.1016/j.ijheatmasstransfer.2017.07.102.
[39] J. Shen, Z. Tu, S.H. Chan, Performance enhancement in a proton exchange membrane fuel cell with a novel 3D flow field, Appl. Therm. Eng. 164 (2020) 114464, https://doi.org/10.1016/j.applthermaleng.2019.114464.
[40] Y. Wang, Optimal design of cathode gas diffusion layer with arrayed grooves for performance enhancement of a PEM fuel cell, Renew. Energy. 199 (2022) 697–709, https://doi.org/10.1016/j.renene.2022.09.011.
[41] X. Zhang, Y. Zhao, L. Xu, Z. Hu, G. Zhao, H. Sun, J. Li, M. Ouyang, Polarization decomposing of proton exchange membrane fuel cell considering liquid water accumulation, J. Electrochem. Soc. 169 (2022) 124517, https://doi.org/10.1149/1945-7111/aca6a8.
[42] Y. Pan, H. Wang, N.P. Brandon, A fast two-phase non-isothermal reduced-order model for accelerating PEM fuel cell design development, Int. J. Hydrogen Energ. 47 (2022) 38774–38792, https://doi.org/10.1016/j.ijhydene.2022.09.044.
[43] P. Antonacci, S. Chevalier, J. Lee, N. Ge, J. Hinebaugh, R. Yip, Y. Tabuchi, T. Kotaka, A. Bazylak, Balancing mass transport resistance and membrane resistance when tailoring microporous layer thickness for polymer electrolyte membrane fuel cells operating at high current densities, Electrochim. Acta. 188 (2016) 888–897, https://doi.org/10.1016/j.electacta.2015.11.115.
[44] Y. Aoyama, Y. Tabe, R. Nozaki, K. Suzuki, T. Chikahisa, T. Tanuma, Analysis of water transport inside hydrophilic carbon fiber micro-porous layers with high-performance operation in PEFC, J. Electrochem. Soc. 165 (2018) F484, https://doi.org/10.1149/2.0801807jes.
[45] H. Naito, K. Ishikawa, T. Sasabe, S. Hirai, T. Tanuma, Investigation of effects of hydrophilic micro-porous layer on liquid water behavior by X-ray imaging, J. Power Sources. 507 (2021) 230285, https://doi.org/10.1016/j.jpowsour.2021.230285.